Negative thermal expansion in the Ruddlesden-Popper calcium titanates

Nathan Z. Koocher,[1] Liang-Feng Huang,[2] and James M. Rondinelli[1,*]

[1]*Department of Materials Science and Engineering, Northwestern University, Evanston, Illinois 60208, USA*

[2]*Key Laboratory of Marine Materials and Related Technologies, Zhejiang Key Laboratory of Marine Materials and Protective Technologies, Ningbo Institute of Materials Technology and Engineering, Chinese Academy of Sciences, Ningbo 315201, China*

(Received 12 August 2020; revised 25 January 2021; accepted 16 April 2021; published 3 May 2021)

Materials exhibiting negative thermal expansion (NTE) are important for the fabrication and operation of microelectronic devices and optical systems. As an important group of Ruddlesden-Popper (RP) perovskites, calcium titanates $Ca_{n+1}Ti_nO_{3n+1}$ [(CTO), $n = 1, 2, \ldots, \infty$] have layered structures and may exhibit quasi-two-dimensional (quasi-2D) NTE within their three-dimensional structural architectures. In this paper, combining density-functional-theory calculations and the self-consistent quasiharmonic approximation method, we investigate the variation of the quasi-2D character of the phonon spectra and thermal expansion in the $Ca_{n+1}Ti_nO_{3n+1}$ family ($n = 1$–3, and ∞) with respect to n. We find that a quasi-2D NTE mechanism is active in the RP-CTOs at n of 1–3, whereas a quasi-rigid-unit mode mechanism is active at $n = \infty$ (i.e., the perovskite phase). We find a NTE trend with layer number for the orthorhombic materials comprising the RP series, but the monoclinic polymorph is an outlier. For the orthorhombic members, we find the critical pressure for NTE increases with increasing n, but the NTE critical temperature decreases (when materials are compared at the same pressure). Additionally, the elastic moduli can be used as effective descriptors for this layer-dependent behavior of the NTE, i.e., the stiffer the RP-CTO then the lower its NTE. We also propose the integrated NTE capacity to capture the correlation between the quasi-2D NTE and n, and it monotonically decreases with increasing n.

DOI: 10.1103/PhysRevMaterials.5.053601

I. INTRODUCTION

Materials with reduced dimensionality are proposed as viable beyond-complementary metal-oxide semiconductor platforms for next-generation electronic devices. Although the few-atom thicknesses possessed by two-dimensional (2D) materials imbue them with unique electronic and thermomechanical properties, it is those same structural features that make 2D materials highly challenging to manufacture, interface, and control with regard to material thickness and sample transfer in nanotechnologies [1]. For these reasons, theoretical material efforts have focused on identifying "thicker" quasi-2D materials with layered crystalline habits that are able to replicate 2D physics by exploiting a dimensional reduction within the active degree of freedom, for example, 2D band structures can be found in three-dimensional (3D) materials if the active electronic orbitals are sufficiently confined [2,3].

In nanoelectronic and optical devices, the accumulated thermal stress from fabrication and during operation may cause component spalling, large resistance variablility, and shifts in photoluminescence [4,5] owing to strain induced by the coefficient of thermal expansion (α, CTE) mismatch between materials, e.g., graphene and its supporting substrate. Hence, thermal properties must be accounted for in both the interpretation of experimental data taken under variable temperature and when processing functional van der Waals heterostructures [6]. Some amount of negative thermal expansion (NTE) may also be beneficial for scaffolding different materials into multicomponent architectures because NTE tends to cancel the unusual deleterious positive expansion and helps reduce the CTE mismatch [7].

NTE is another unique 2D property exhibited by graphene, germanene, blue phosphorene [8], and transition-metal dichalcogenides [9]. Layer number was found to control the thermal expansion in the graphene-graphite-diamond carbon allotrope family [10]. Negative thermal expansion was found to decrease in magnitude as layer number increased: Graphene (monolayer) exhibits a larger negative α and temperature range than graphite (two layers), whereas diamond (3D connected) exhibits only positive thermal expansion. The underlying negative thermal expansion mechanism in this family is a two-dimensional Z-acoustic (ZA) phonon mode associated with quadratic dispersion in momentum space. The ZA mode exhibits a negative Grüneisen parameter in graphene and graphite (albeit, smaller magnitude in graphite), yielding the negative thermal expansion.

Negative thermal expansion mechanisms in 3D ternary perovskite-type materials are due to one of the three general microscopic mechanisms: phase-transition-driven (structural [11] or electronic/magnetic [12]), phonon-driven [13], or elasticity-driven [14,15] (negative compliance tensor elements) NTE. For phonon-based mechanisms, NTE arises from a population of the modes exhibiting negative mode-Grüneisen values ($\gamma = -\frac{V}{\nu}\frac{d\nu}{dV} < 0$), a lattice-dynamical quantity which describes the change in phonon frequency ν of a particular mode with unit-cell volume V [16]. A phonon with $\gamma < 0$ usually exhibits transverse atomic

*jrondinelli@northwestern.edu

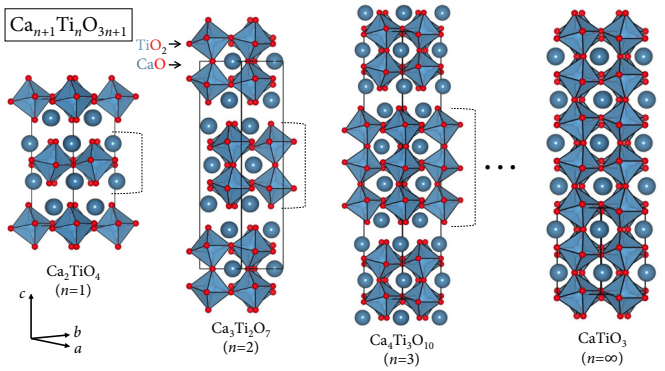

FIG. 1. Atomic structures of the homologous series of Ruddlesden-Popper $Ca_{n+1}Ti_nO_{3n+1}$ titanates. The broken brackets indicate the number (n) of TiO_6 octahedral layers.

displacements in its corresponding vibrational pattern, which justifies the so-called tension effect [17,18]. In the aforementioned 2D materials, this behavior manifests as the ZA mode (i.e., graphene), whereas in 3D framework materials (i.e., with nearly rigid octahedra), it occurs as collective rotations and tilts of polyhedra—so-called rigid unit modes (RUMs). In fact, d'Ambrumenil and colleagues showed that 2D structural units within the 3D framework structure $ZnNi(CN)_4$ allows both 3D-RUMs and 2D-transverse-vibration-type phonons to contribute to the NTE [19], although the transverse vibration (hence, the 2D mechanism) was identified to dominate. Negative thermal expansion driven by lattice dynamics, however, occurs over specific temperature ranges, i.e., when thermal population of the modes that yield negative γ dominate over those with positive γ (and $\gamma > 0$ arises from a bond-stretching effect) [18]. Microscopically, when atomic bonds involved in a vibration are strong, the bond stretching outcompetes the bond bending modes, resulting in positive γ contribution. In contrast, if the bonds are weak, then the bending contribution dominates to give negative γ.

Owing to its variable number of perovskite blocks, the Ruddlesden-Popper (RP) series is an ideal family to explore the effect of dimensionality on NTE. The $n = 1$ member exhibits a quasi-2D structure with a sheet of corner-connected BO_6 octahedral units (in the [100] and [010] directions) separated by rocksalt layers along the [001] direction, whereas the $n = \infty$ member, the perovskite, exhibits a 3D structure with corner-connected octahedra in all directions as shown for $Ca_{n+1}Ti_nO_{3n+1}$ in Fig. 1. The effect of dimensionality on the properties of all inorganic RP oxides has been studied recently in the Sr-Ti-O homologous family: It was found, for example, that the band gaps decrease as n increases due to decreased confinement [20,21], the exciton binding energy tends to decrease as n increases [21], and strain can induce a two-to-three-dimensional ferroelectric transition [22]. Layer-dependent phase stabilities and thermal expansion behavior were also investigated with a dimensionality transition occurring at $n = 3$ due to the appearance of octahedral rotations in those structures ($n \geqslant 3$) [23]. The optical properties as a function of dimensionality have also been studied experimentally in $Ca_3Ti_2O_7$ and $CaTiO_3$ [24].

Pressure-induced volumetric negative thermal expansion was previously demonstrated in the polar polymorphs of $Ca_3Ti_2O_7$, the $n = 2$ member of the Ca-Ti-O homologous series, enabled by a quasi-2D vibration [25]. Bansal and colleagues [26] then performed a combined experiment-theory study to investigate the quasi-2D nature of the dispersion using inelastic x-ray scattering (IXS) and density functional theory (DFT). Although the IXS data showed only linear dispersion behavior, their relaxed DFT calculation showed quasi-2D dispersion behavior. The difference was attributed to the lack of anharmonic effects in the DFT calculation [26]. Uniaxial NTE was also demonstrated in $Ca_3Mn_2O_7$ and $Ca_{3-x}Sr_xMn_2O_7$, attributed to a symmetry-trapped rigid unit phonon in the high-temperature centrosymmetric phase (*Acaa* symmetry) [27,28]. The latter trapping phenomenon was then investigated in $n = 1$ Ca_2GeO_4 as a model system with density functional calculations, and it was determined that anisotropy in the mechanical compliance tensor and phonons with $\gamma < 0$ were responsible for the *uniaxial* NTE in the $I4_1/acd$ phase [14]. This result reinforces the importance of phonon modes with negative Grüneisen parameters as in the $n = 2$ RPs but further highlights the role of an anisotropic elastic compliance tensor in the thermal response. The anisotropy in the elastic compliance arises from the "frozen-in" octahedral distortions and symmetry-breaking rocksalt motif in the RP series.

The elastic compliance tensor was also analyzed as a function of n in the Ca-Ge-O homologous series. The anisotropy was found to decrease as a function of n [29]. The $n = 1$ germanate exhibited the most anisotropic tensor and, thus, the strongest predicted *uniaxial* NTE [29]. The behavior was attributed to the increased interface fraction in the small-n compounds. Finally, the uniaxial CTE was tuned by chemical control over the tolerance factor in $Ca_{2-x}Sr_xMn_{1-y}Ti_yO_4$ where maximal uniaxial negative thermal expansion behavior was found preceding a low-tolerance factor phase boundary ($I4_1/acd \rightarrow Pbca$) due to progressively lower frequencies of octahedral rotations and just before a high-temperature phase boundary ($I4_1/acd \rightarrow I4/mmm$) due to high elastic compliance [30]. Taken together, the aforementioned uniaxial NTE results suggest design strategies for NTE in RP compounds by: (i) controlling proximity to a phase transition, (ii) increasing the elastic anisotropy arising from static octahedral distortions, and/or (iii) increasing the interface fraction (low-n compounds). It should be noted, however, that the uniaxial work presents a different physical picture than that presented here (and previously in our earlier $n = 2$ work). The uniaxial research focuses on interaxis coupling and elastic anisotropy, whereas we focus on quasi-2D and quasi-3D mechanisms.

Here, we computationally assess the structural, lattice dynamical, and thermal properties of the calcium titanate RP series with layer thickness $n = 1$–3, and ∞ within the framework of density functional theory and identify the phononic origin of their volumetric negative thermal expansion. As the $n = 1$ phase has not been synthesized experimentally, we propose structures which may be targets for synthesis: ambient pressure *Pbca* and $P2_1/c$ phases and a high-pressure *Cmca* phase. All RP structures exhibit NTE due to the quasi-2D mechanisms, whereas the perovskite phase exhibits NTE due to a quasi-RUM. We find that, for the orthorhombic

compounds, the volumetric NTE capacity increases as n decreases, which can be understood to arise from a decrease in the elastic stiffness of the materials with n. The monoclinic angle in $P2_1/c$ hinders the NTE response such that a higher critical pressure is needed to activate the phenomena than in the $n = 1$ *Pbca* and the $n = 2$ members. We find that the *Pbca* phase at $n = 1$ has the largest negative CTE of -2.5×10^{-6} K^{-1} (at $P = 20$ GPa, $T = 55$ K) and exhibits NTE over the largest temperature range (up to 149 K). To compare NTE behavior across materials, we use the NTE capacity, which reveals that the NTE behavior increases as n decreases owing to the increased mechanical stiffness in the orthorhombic members. These models provide a strategy to understand and design NTE in a variety of layered transition-metal compounds.

II. MATERIALS AND METHODS

A. $Ca_{n+1}Ti_nO_{3n+1}$ structures

Figure 1 shows the Ruddlesden-Popper and perovskite structures comprising the Ca-Ti-O homologous series examined in this paper. An interesting feature of this structural family is the presence of inversion symmetry with layer number n. Members with values of n even are predicted to be polar due to the odd number of CaO layers and their noncanceling antipolar displacements of the Ca cations [31]. Conversely, odd-n members are predicted to be nonpolar because they have an even number of CaO layers, and, thus, antipolar A-site displacements are fully compensated.

The low-temperature phase of perovskite $CaTiO_3$ ($n = \infty$) exhibits *Pnma* symmetry with the $a^-a^-c^+$ tilt pattern (in Glazer notation [32]), and it undergoes two phase transitions upon heating at ambient pressure. It undergoes an orthorhombic-to-tetragonal transition ($Pbnm \rightarrow I4/mcm$) at 1512 ± 13 K followed by a transition to cubic $Pm\bar{3}m$ symmetry at 1636 ± 12 K [33,34]. At all temperatures, the structure is centrosymmetric. Pressure-dependent x-ray diffraction measurements show that the orthorhombic *Pbnm* phase is stable up to 60 GPa. After 40 GPa, however, peaks broadened in the x-ray pattern, which was attributed to nonhydrostatic stress [35]. This experimental result is consistent with *ab initio* molecular dynamics calculations that also find dynamic stability of the orthorhombic polymorph up to 65 GPa at 300 K [36].

$Ca_4Ti_3O_{10}$ ($n = 3$) crystallizes in the centrosymmetric *Pbca* symmetry (space-group number 61) at room temperature [37] and exhibits the $a^-b^-c^+$ tilt pattern. Its temperature-pressure phase diagram has not been investigated experimentally. $Ca_3Ti_2O_7$ ($n = 2$) exhibits polar $Cmc2_1$ symmetry, which is stable up to 1150 K [27] and is a hybrid improper ferroelectric [38].

The $n = 1$ member of the family, Ca_2TiO_4, remains to be synthesized experimentally and is predicted to be thermodynamically unstable based on disproportionation energies [39], indicating that the decomposition products are RP titanates of increased layer number (i.e., $n = 2$ or $n = \infty$) and CaO. It also does not appear in the phase diagram for the Ca-Ti-O system [40–43].

To search for candidate $n = 1$ structures, we employ symmetry-based structure searching, aided by Bayesian inference. A previous result by Balachandran *et al.* [44] enumerated common distortions in experimentally known $n = 1$ RP oxide compounds. The commonly observed distortions for Ca on the A site transform as the irreducible representations (irreps) $X_2^+ \oplus X_3^+$ and P_4, whereas Ti on the B site frequently exhibits the distortion transforming as $X_3^+ \oplus M_3^-$ where each mode eigenvector is an irrep of the $I4/mmm$ space group. Additionally, low-temperature distortions adopted by $n = 1$ RP oxides with these elements include $X_2^+ \oplus X_3^+$ and P_4. As $X_2^+ \oplus X_3^+$ and P_4 appeared twice, we checked the stability of the structures produced by these irreps with DFT calculations described below: *Pbca* ($X_2^+ \oplus X_3^+$) and $Pca2_1$ ($X_2^+ \oplus X_3^+ \oplus P_4$).

We found that *Pbca* was nearly dynamically stable, whereas $Pca2_1$ was dynamically unstable. Upon compression by approximately 10%, the octahedral rotation in *Pbca* was no longer favorable, leading to Ca_2TiO_4 with the *Cmca* space group and one octahedral tilt. Tracking the DFT-computed lattice constants with pressure shows clear evidence of a phase transition (Fig. S4 of the Supplemental Material (SI) [45]). We then relaxed the *Cmca* structure to obtain its equilibrium geometry and found it exhibits three unstable modes at the Γ point (see Figs. S1 and S6 in the SI appearing as Ref. [45]). After condensing the unstable modes, we found that although the *Pbca* structure was lowest in energy, it was not dynamically stable [45]. The second-lowest-energy $P2_1/c$ polymorph was dynamically stable and is approximately 8 meV/formula unit higher in energy than the *Pbca* phase, which is within kT at 300 K. We then computed the thermomechanical properties of both phases and herein focus on the *Pbca* phase for comparison in the Ca-Ti-O orthorhombic RP and perovskite series because it is lowest in energy and is of the same crystal class as the other materials. We then compare the $n = 1$ *Pbca* and $P2_1/c$ polymorphs directly. Our phase exploration of Ca_2TiO_4 suggests that a synthesis experiment under pressure may yield the *Cmca* phase, and subsequent decompression experiments could yield an ambient pressure polymorph. This synthetic strategy has successfully yielded novel intermetallics [46–49] and alloys [50].

B. Density functional calculations

DFT calculations were performed using the Vienna *ab initio* software package [51,52] with projector augmented plane-wave pseudopotentials [53,54] and the Perdew-Burke-Ernzerhof exchange-correlation functional revised for solids [55,56]. The valence configurations for Ca, Ti, and O are $3s^23p^64s^2$, $3p^63d^24s^2$, and $2s^22p^4$, respectively. An 800-eV energy cutoff was used for the plane-wave expansion for all structures. A $6 \times 6 \times 6$ Γ-centered k-point mesh was used for $CaTiO_3$, $6 \times 6 \times 1$ Γ-centered mesh for $Ca_4Ti_3O_{10}$ and Γ-centered $8 \times 8 \times 2$ mesh for Ca_2TiO_4 (*Pbca*). In addition, a Γ-centered $6 \times 6 \times 2$ mesh was used for the *Cmca* phase and a Γ-centered $6 \times 6 \times 6$ mesh was used for the $P2_1/c$ phase. Gaussian smearing (0.1-eV width) was used for each structure. The electronic convergence threshold was 5×10^{-8} eV, and the force convergence threshold for atomic relaxations was 5×10^{-4} eV Å^{-1}. The stresses after structural relaxation were less than 0.05 kbar. A comparison of theoretical and experimental structures are available in Tables S1– S4 of the

SI [45], and energetic comparisons of the $n = 1$ polymorphs are in Table S5 of the SI in Ref. [45].

C. Lattice dynamical properties

The lattice dynamical properties were calculated using the finite-displacement method with pre- and postprocessing utilizing the PHONOPY software package [57]. An atomic displacement of 0.03 Å is used for $CaTiO_3$, $Ca_4Ti_3O_{10}$, and Ca_2TiO_4. Supercell sizes of $2 \times 2 \times 2$ (160 atoms) for $CaTiO_3$, $2 \times 2 \times 1$ (272 atoms) for $Ca_4Ti_3O_{10}$, $4 \times 4 \times 1$ (448 atoms) for Ca_2TiO_4 (*Pbca*), and $2 \times 2 \times 2$ supercell (112 atoms) of the AFLOW [58] primitive cell for Ca_2TiO_4 ($P2_1/c$) were used to obtain phonon spectra to assess thermodynamic quantities using the self-consistent quasiharmonic approximation (SC-QHA) method [59]. Computational details for $n = 2$ $Ca_3Ti_2O_7$ can be found in Ref. [25]. A $2 \times 2 \times 1$ cell (112 atoms) was used for the $n = 1$ *Cmca* Ca_2TiO_4 phase from which the $n = 1$ phase space was searched. The $n = 1$ $Cmc2_1$ phonon spectra were generated using a $2 \times 2 \times 2$ supercell (112 atoms) of the AFLOW [58] primitive cell. Here we note that phonon dispersions obtained from the finite-displacement method for Ca_2TiO_4 (*Pbca*) were sensitive to the choice of numerical parameters in our calculation (see Fig. S5 of the SI in Ref. [45] for additional details); the quadratic-dispersing phonon was generated using a $2 \times 2 \times 1$ supercell. Also, the $n = 3$ structure presented a numerical instability in the equilibrium structure (see Fig. S4 of the SI) [45], therefore, compressed structures corresponding to approximately 7.5–10% of the equilibrium value were used to generate the thermal expansion data with the SC-QHA. Justification for this can be found in the SI, Sec. VI B and Figs. S9– S11 [45].

D. The quasiharmonic approximation and the SC-QHA method

The SC-QHA method allows for the efficient calculation of anharmonic (i.e., thermodynamic) properties of solids based on *ab initio* electronic and lattice dynamical input. The most common way to obtain these properties is to use the QHA method, where phonon frequencies are volume dependent but not explicitly temperature dependent. Temperature dependence only occurs indirectly through thermal expansion effects [57,60,61]. The conventional QHA implementation is very time consuming. Phonon spectra of ten or more volumes of a compound are needed to obtain an accurate free energy-volume relationship, from which thermodynamic properties (including thermal expansion) are derived. This necessitates stable phonon spectra at each volume. The ground state and expanded volumes of some oxides and perovskites, however, may have artificial imaginary phonon modes at the DFT level [23,59]. For example, $SrTiO_3$ exhibits imaginary modes in its DFT equilibrium and expanded volume structures [23] and $Ca_3Ti_2O_7$ exhibits imaginary modes in its expanded volumes [25,59]. The presence of such imaginary modes thereby prohibits the QHA method from being applied.

The SC-QHA method, on the other hand, only requires phonons at three volumes of a material in order to obtain thermodynamic quantities. Thus, if imaginary modes appear at equilibrium or expanded volumes of a material, three compressed volumes can be used instead. Because those artificial imaginary modes in reality should be real and exhibit a smooth dependence on volume, phonon frequencies of the three compressed volumes are extrapolated and used to replace the problematic modes at the equilibrium or expanded volume. (Note that negative phonon modes are not allowed as a solution in the SC-QHA method.) This is the main difference between the SC-QHA and the QHA, which has led to the success of the SC-QHA in modeling accurate CTEs for perovskite-structured titanates [23,25,59]. We also found that the SC-QHA yields good agreement between the 0-K DFT-computed equilibrium volumes of the materials and the 1.0 K (i.e., lowest computed temperature) volume from the SC-QHA method, supporting the validity of our following thermomechanical results (see SI Sec. VI A and Fig. S8 [45]).

The derivation and validation of the SC-QHA method is presented in Ref. [25]. Here, we briefly summarize the algorithm, which solves for the equilibrium volume at a specified pressure and temperature as

$$V(P,T) = \left[\frac{dE_e}{dV} + P\right]^{-1} \frac{1}{N_q} \sum_{q,\sigma} U_{q,\sigma}\gamma_{q,\sigma}, \qquad (1)$$

where $U_{q,\sigma}$ is the internal energy and $\gamma_{q,\sigma} = -\frac{V}{\nu_{q,\sigma}}\frac{d\nu_{q,\sigma}}{dV}$ is the Grüneisen parameter of phonon mode (q,σ). The number of q-grid points is N_q, σ is the phonon branch, and q is the phonon wave vector. Equation (1) shows that the volume is obtained by balancing external and internal pressures $P = P_e(V) + P_\gamma(V,T)$ where $P_e = -\frac{dE_e}{dV}$ is the electronic pressure and $P_\gamma = \frac{1}{VN_q}\sum_{q,\sigma} U_{q,\sigma}\gamma_{q,\sigma}$ is the phononic pressure.

In practice, electronic energies (E_e) are obtained first for ten (or more) volumes using DFT. Then an equation of state, such as the fifth-order Birch-Murnaghan is fit to the calculated E_e values. Next, phonon spectra of two or three volumes are calculated to obtain the first-order or second-order Taylor expansion of the phonon frequencies, respectively, of the form

$$\nu(V) = \nu(V_0) + \left(\frac{d\nu}{dV}\right)_0 \Delta V + \frac{1}{2}\left(\frac{d^2\nu}{dV^2}\right)_0 \Delta V^2, \qquad (2)$$

where $\Delta V = V - V_0$ and V_0 is the reference volume. An assumption here is that $\nu(V)$ is continuous and differentiable. The volume-dependent Grüneisen parameter is then,

$$\gamma(V) = -\frac{V}{\nu}\left[\left(\frac{d\nu}{dV}\right)_0 + \frac{1}{2}\left(\frac{d^2\nu}{dV^2}\right)_0 \Delta V\right]. \qquad (3)$$

The self-consistent loop used to obtain $V(P,T)$ is initialized at a certain temperature by setting the initial volume to be 0.2% larger than the DFT equilibrium volume. New volumes, phonon frequencies, and Grüneisen parameters are updated at that temperature until convergence is reached within a threshold (e.g., 10^{-6}). Then the temperature window is scanned where calculated volumes, phonons, and Grüneisen parameters at one temperature are used as initial values for the next temperature. After converging these phonon parameters, thermodynamic properties, such as the thermal expansion coefficient can be calculated. The method assumes nonnegative phonon frequencies as well as a smooth $\nu - V$ relationship. The method is available online [62] and as part of AFLOW [63].

For the Ca-Ti-O data presented in this paper, a fifth-order Birch-Murnaghan equation of state is used for fitting [64]. These data are available in Table S6 and Figs. S2 and S3 of the SI [45]. In addition, we note that because Ca_2TiO_4 ($n = 1$) and $Ca_4Ti_3O_{10}$ ($n = 3$) exhibit unstable phonons at certain unit-cell volumes (see Figs. S5 and S7 of the SI, Ref. [45]), the conventional QHA cannot be used to calculate the anharmonic lattice properties, such as

$$\alpha = \frac{1}{V}\frac{dV}{dT} = \frac{1}{N_q V_T B_T}\sum_{q,\sigma} C_V^{q,\sigma}\gamma_{q,\sigma}, \tag{4}$$

where σ, q, and N_q have been defined previously, B_T is the isothermal bulk modulus, C_V is the isovolume heat capacity, and γ is the Grüneisen parameter. The q grid for the RP compounds (except the $P2_1/c$ phase) was $4 \times 4 \times 1$, whereas the grid for the perovskite and $n = 1$ $P2_1/c$ was $4 \times 4 \times 4$. The thermomechanical properties presented here were calculated with the second-order SC-QHA formulism (2nd-SC-QHA).

Note that the external pressure term is an independent parameter in the SC-QHA used to solve for the volume at that specified pressure (and temperature) [25]. To find the critical pressure, we parametrically varied P to find the value for which $\alpha < 0$. The minimum pressure that provides this constraint is then identified as the critical pressure p_c.

III. RESULTS AND DISCUSSION

A. Equilibrium structures

We first compare the bond and lattice stiffness of the Ca-Ti-O homologous series in terms of changes in atomic structure features and the macroscopic elastic responses using our DFT relaxed atomic structures. Detailed crystallographic information is available in the SI of Ref. [45], and here we note that there is good agreement between the DFT atomic structures and those from experiment. A comparison among $Ca_3Ti_2O_7$, $Ca_3Zr_2O_7$, and $Sr_3Zr_2O_7$, previously proposed that weaker B-O and A-O bonds make it easier to observe NTE using pressure in layered RP oxides [25]. This suggests that compounds with stiffer or stronger metal-anion bonds will exhibit reduced (or zero) NTE response. We now assess whether this hypothesis is valid in $Ca_{n+1}Ti_nO_{3n+1}$ titanates.

Figure 2(a) shows that the average (total) bond length evolves with a volcanolike dispersion with inverse layer number ($1/n$) and is maximum at $n = 2$ ($Ca_3Ti_2O_7$). To understand this behavior, we next decomposed the average bond length into the average equatorial [Fig. 2(b)] and axial [Fig. 2(c)] bond lengths. Here we find that generally the average equatorial bond lengths decrease and the average axial bond lengths increase as n decreases. For both types of bonds, we find that the dispersion with n is different over the ranges $n \in [1, 2]$ and $n \in [3, \infty]$. This change originates in the fact that the TiO_6 octahedral network transitions from the 3D character in the $n = \infty$ perovskite, to mixed dimensional (3D and 2D characters) in the $n = 3$ compound, and finally presents exclusively 2D character in the $n = 1$ and 2 materials. The reduced dimensionality leads to axial oxide anions that are terminal ligands (one coordinate) and, thus, exhibit, on average, larger bond lengths. As a consequence, the average TiO_6 octahedral volume [Fig. 2(e)] and in-plane area of the

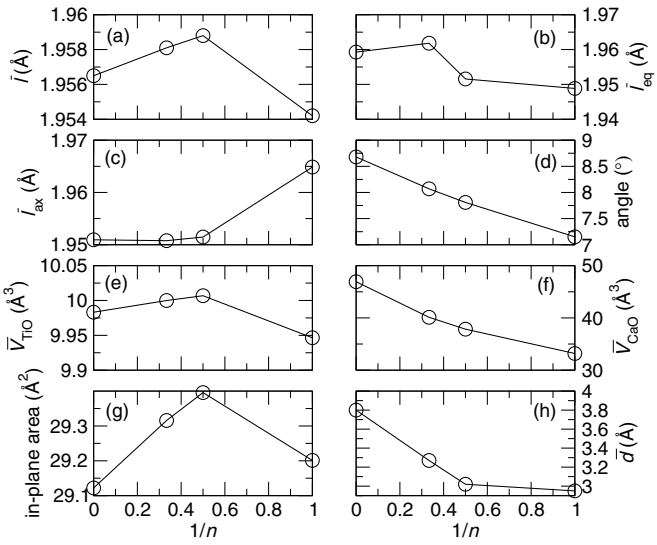

FIG. 2. Structural features of the $Ca_{n+1}Ti_nO_{3n+1}$ titanates as a function of inverse layer number $1/n$: (a) average (total) Ti-O bond length, (b) average Ti-O equatorial bond length, (c) average Ti-O axial bond length, (d) average TiO_6 rotation angle about [110], (e) average TiO_6 octahedral volume, (f) average CaO_x polyhedral volume, (g) in-plane area of the (001) plane ($a \times b$), and (h) average Ca-Ca distance along [001].

(001) plane, obtained as the product of the a and b lattice parameters [Fig. 2(g)], exhibit maxima at $n = 2$.

On the other hand, the average rotation angle about [110] [Fig. 2(d)], average Ca-O polyhedral volume [Fig. 2(f)], and average interplanar Ca-Ca spacing [Fig. 2(h)] exhibit monotonic dependencies with n. Each structural feature increases toward the perovskite value, which we attribute to the decreased interface fraction of CaO rocksalt layers as n increases. More octahedral units with 3D corner connectivity act to constrain the average rotation angle of the TiO_6 octahedra. The interface also undercoordinates the A-site Ca, resulting in a lower Ca-O polyhedral volume as n decreases. The CaO_x polyhedra were modeled using a maximum bond length of 4 Å, yielding CaO_{12} in the perovskite-type layers and CaO_9 at the rocksalt interface in each RP structure. The interplanar spacing decreases as n decreases as well so as to maximize coordination of the Ca atoms. As more layers of octahedra are added from $n = 1$ to 3, the Ca atoms become fully coordinated within an AO_x perovskitelike polyhedron, and, thus, the Ca cations shift to become further apart along the z axis to maintain the same nominal bond valence. This shift leads to an increase in the average spacing.

As there was no clear stiffness trend from a bond analysis of the homologous Ca-Ti-O series, we next calculated the elastic stiffness tensor C_{ij} and the bulk modulus B to ascertain the extent of anisotropy in the linear mechanical properties (Fig. 3). Most tensor components as well as the bulk modulus increase with n. We find that the out-of-plane moduli, C_{33} increase from 229 to 343 GPa as n increases as does the bulk modulus (from 130 to 180 GPa). Thus, as TiO_6 octahedral layers increase from $n = 1$ to ∞, the lattice becomes stiffer in that direction. Interestingly, the in-plane stiffness (C_{66}) for the $n = 1$ compound is higher than that of the $n = 2$ compound,

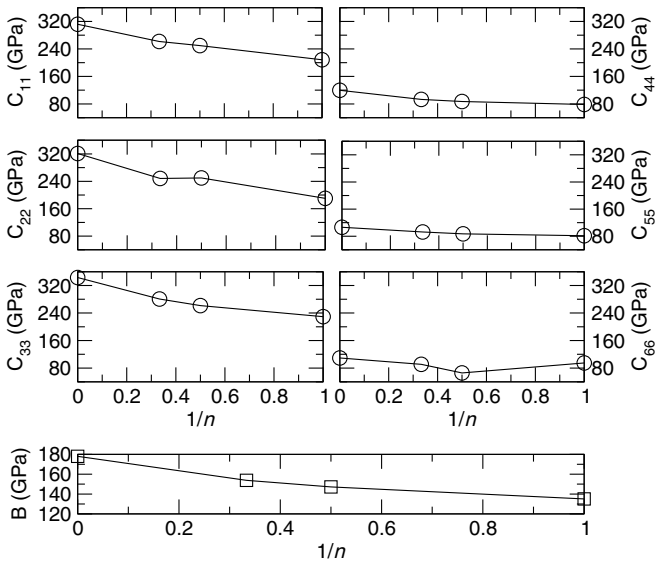

FIG. 3. Components of the elastic stiffness tensor C_{ij} and bulk modulus B as a function of inverse layer number $(1/n)$.

indicating the monolayer is less susceptible to a shear distortion. Similarly, $n = 3$ has an odd number of octahedral units and may not be easily sheared. The octahedra in perovskite are 3D corner connected, so as expected, the in-plane stiffness is highest for that phase.

B. Phonon dispersions

Figure 4 shows the phonon dispersions for $Ca_{n+1}Ti_nO_{3n+1}$ with $n = 1$–3, and ∞ along the $k_z = 0$ plane of the Brillouin zone. As expected, all structures exhibit three acoustic modes that approach zero frequency at the zone center. Remarkably, Ca_2TiO_4 [Fig. 4(a)] and $Ca_3Ti_2O_7$ [Fig. 4(b)] exhibit quadratic-dispersing acoustic branches along the Γ-X path, whereas the $n = 3$ [Fig. 4(c)] and perovskite [Fig. 4(d)] titanates exhibit the expected linearly dispersing acoustic branches along this direction. The quadratic dispersions are also observed in 2D materials, such as graphene and graphite

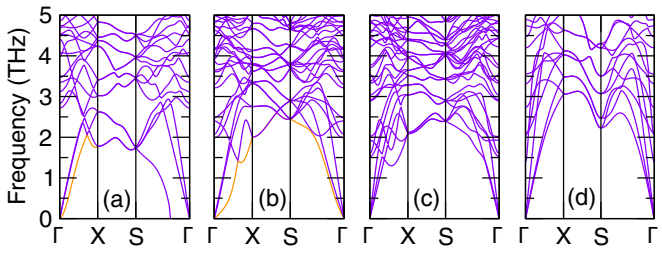

FIG. 4. Phonon dispersions of (a) Ca_2TiO_4, (b) $Ca_3Ti_2O_7$, (c) $Ca_4Ti_3O_{10}$, and (d) $CaTiO_3$. The $n = 1$ and 2 structures in (a) and (b) exhibit phonons with 2D character, indicated by an orange (bold) line. The chosen path in momentum space spans the planar portion of the structure consistent with where phonons responsible for NTE in 2D materials occur. The $n = 1$ dispersion for the *Pbca* phase is slightly dynamically unstable along the Γ-S path. For in-depth analysis of this, see Fig. S5 of the SI and associated discussion in Ref. [45].

where a ZA phonon with quadratic dispersion occurs along an in-plane trajectory in the Brillouin zone. This ZA mode exhibits $\gamma < 0$ and is responsible for the NTE. A parabolic ZA mode was also responsible for negative thermal expansion in single-layer MoS_2 [65]. Note that although a quadratic dispersion of the ZA mode indicates susceptibility of a material to exhibit NTE, it is only a sufficient rather than necessary condition. We show in the following that the phonon dispersions of the titanates suggests a 2D mechanism enabling (pressure-tunable) negative thermal expansion for $n = 1$, but potentially a RUM mechanism for $n = 3$ and perovskite.

Owing to the quadratic dispersion of the ZA phonon mode in $n = 2$ $Ca_3Ti_2O_7$, which arises from severing the octahedral connectivity, we expected that the layered $n = 1, 3$ members would exhibit a similar feature whereas the 3D-connected $n = \infty$ perovskite should exhibit linearly dispersion. As we see next, the 2D mechanism is active when γ of that low-energy mode is negative regardless of the specific curvature of band.

C. Thermal expansion

Figure 5 shows the pressure-dependent thermal expansion coefficients for Ca_2TiO_4, $Ca_3Ti_2O_7$, $Ca_4Ti_3O_{10}$, and $CaTiO_3$ as calculated with the 2nd-SC-QHA. As these are anisotropic materials, it should be noted that the calculated volume expansion coefficients are performed in a partially anisotropic manner because the phonon spectra used to generate the thermal expansion coefficient were from DFT calculations wherein the unit-cell shape was optimized. Although this treatment neglects internal coupling between different lattice vectors (i.e., Poisson ratio), it is justified because in the RP Sr-Ti-O series, the volumetric thermal expansion coefficients from partially and fully anisotropic methods are nearly the same in the 0–900-K temperature range [23]. We find that all materials exhibit $\alpha > 0$ at ambient pressure (0 GPa) and a transition to $\alpha < 0$ with applied hydrostatic pressure. Note that the thermal expansion coefficient for $CaTiO_3$ agrees well with experiment (see Fig. S19 of the SI of Ref. [45]). The different temperature ranges over which NTE exists as a function of n and pressure are explored later. We note that our prediction of negative thermal expansion can be experimentally verified as this property has been investigated under similar pressures for $MgSiO_3$ [66,67], indium [68], and ϵ-Fe [69], as well as under high pressure, low temperatures in indium [70], and ϵ-Fe [71]. Next, we emphasize that despite the absence of a quadratically dispersing acoustic phonon for $n = 3$ and $n = \infty$, NTE occurs in all calcium titanates. Thus, a quadratic dispersing phonon is a signature of but not a necessary condition for NTE.

To understand the existence of NTE at ambient pressure, we examine the mode Grüneisen dispersions for the Ca-Ti-O homologous series, focusing on the modes that have negative Grüneisen parameters and, thus, lead to negative thermal expansion. Figure 6 shows the Grüneisen dispersions for the $n = 1$–3 and ∞ members of the series. First, we find each material exhibits negative Grüneisen parameters. The eigenvectors corresponding to the dominant modes exhibiting negative Grüneisen parameter for each material are presented in Figs. S12– S16 of the SI of Ref. [45]. The $n = 1$–3 (orthorhombic) compounds have a ZA or transverse acoustic (TA) mode hybridizing with a shearing optical (SO) mode,

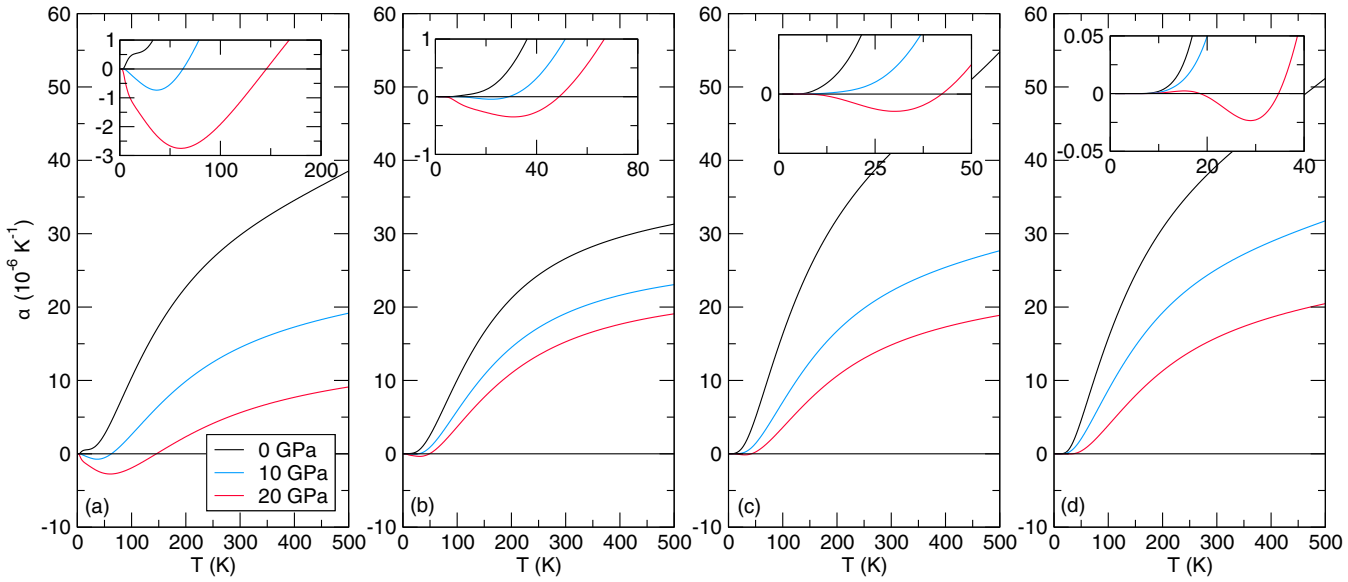

FIG. 5. Thermal expansion coefficients for (a) Ca_2TiO_4, (b) $Ca_3Ti_2O_7$, (c) $Ca_4Ti_3O_{10}$, and (d) $CaTiO_3$. All materials have pressure-induced negative thermal expansion and a CTE that decreases with pressure at high temperatures due to bulk modulus stiffening (see Fig. 8). The insets span the low-temperature ranges for which NTE occurs.

whereas the perovskite compound has a TA mode that mixes with a longitudinal acoustic (LA) mode. The $n = 1$ monoclinic structure has hybridization of its ZA and LA modes. Our analysis of the eigenvectors corresponding to the modes with negative Grüneisen parameter reveals that the quasi-2D mechanism reported in Huang *et al.* [25] is also active in the $n = 1$–3 structures. The mode mixing transfers the quasi-2D Z displacements from the ZA mode to the optical modes and gives rise to low-temperature NTE as we show below.

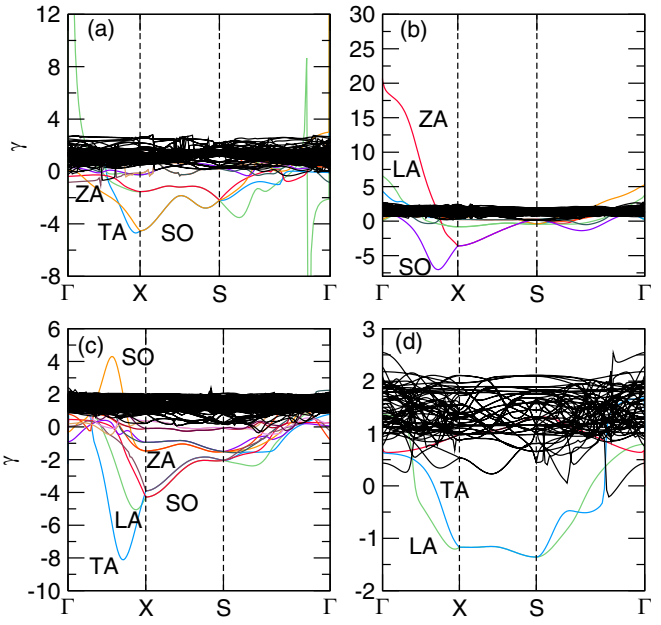

FIG. 6. Grüneisen spectra for (a) Ca_2TiO_4, (b) $Ca_3Ti_2O_7$, (c) $Ca_4Ti_3O_{10}$, and (d) $CaTiO_3$. Important modes are highlighted, e.g., ZA (red, all plots), TA (blue, all plots), LA (green, all plots), and SO (various, all plots).

In contrast, the modes with negative Grüneisen parameters in perovskite $CaTiO_3$ exhibit quasi-RUM behavior whereby the shared (bridging) oxygen atoms in the octahedra exhibit transverse vibrations as a result of concerted tilts and rotations of the rigid polyhedra with small perturbations to the regular unit. This behavior is seen in ZrV_2O_7 [18] in contrast to the ideal-RUM behavior (no distortions to the polyhedra) as reported in ZrW_2O_8 [18] and ScF_3 [72]. The quasi-RUM pattern also appears as part of two shearing modes in the $n = 3$ structure that yield negative Grüneisen parameters. The TiO_6 octahedral unit of the trilayer has rotation and tilt motion (see the animation provided in the SI Ref. [45]). This demonstrates that the 2D NTE mechanism coexists with the quasi-RUM mechanism, and that the dimensionality crossover of the NTE mechanism occurs in the $n = 3$ phase.

Figure 6 shows that the ZA mode undergoes a transition from positive-to-negative γ along the Γ to X path, whereas it is already negative at Γ in the $n = 1$ compound. The positive-to-negative transition is attributed to stretching of weak interlayer bonds induced by the ZA mode [25]. This feature (positive-negative transition) is active in the γ of $n = 2$ and 3 titanates, which have multiple octahedral layers connected to each other in the z direction, but is inactive in $n = 1$ where there is only one octahedral layer interleaved with rocksalt layers. Figure 3 supports the role played by the weak interlayer bonds in $n = 1$ where the moduli of the elastic stiffness tensor along the z direction (C_{33}, C_{44}, and C_{55}) increase as $n \to \infty$. The octahedral layers in Ca_2TiO_4 ($n = 1$) exhibit weaker bond stretching along z compared to the other members in the series.

Next, we focus on the NTE regions of the titanates. At low temperatures, the quasi-2D and quasi-RUM mechanisms dominate, leading to negative thermal expansion because only the low-frequency modes with negative Grüneisen parameter are excited. The negative-to-positive transition occurs in the coefficient of thermal expansion for each material because

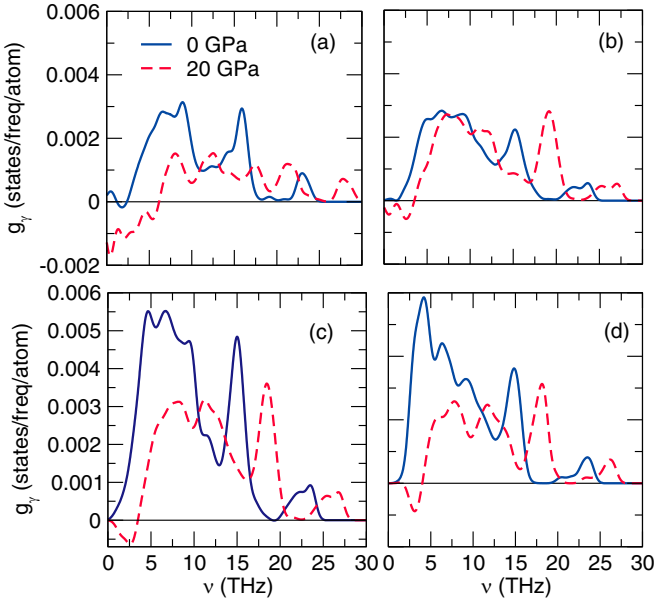

FIG. 7. The variations in Grüneisen-weighted phonon density-of-states g_γ with pressure for (a) Ca_2TiO_4, (b) $Ca_3Ti_2O_7$, (c) $Ca_4Ti_3O_{10}$, and (d) $CaTiO_3$.

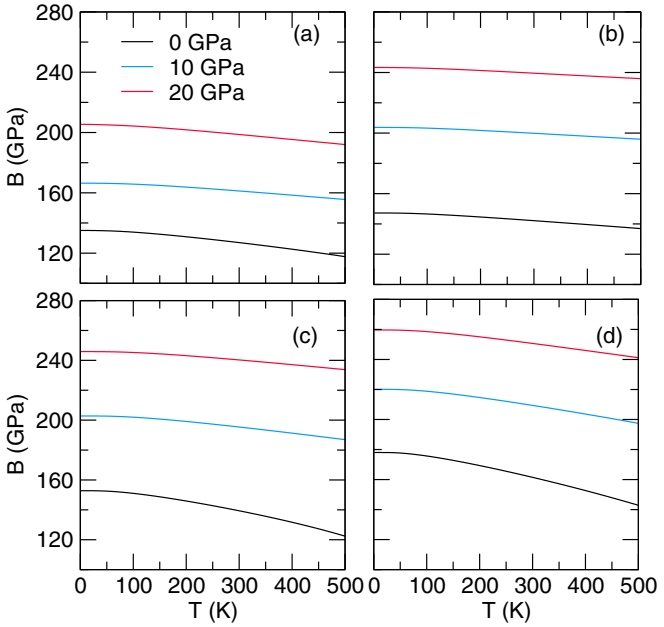

FIG. 8. Bulk modulus as a function of temperature for (a) Ca_2TiO_4, (b) $Ca_3Ti_2O_7$, (c) $Ca_4Ti_3O_{10}$, and (d) $CaTiO_3$. All titanates show an increased bulk modulus with pressure, i.e., bulk modulus stiffening.

increasing temperature allows more phonons with the positive Grüneisen parameter to be excited. Evidence for this is seen in Fig. 7 as there is only positive Grüneisen density of states (DOS) at higher frequencies.

Furthermore, we find that the critical pressures p_c at which NTE first arises increase as layer number n increases (Table I). The critical temperatures T_c at which $\alpha(T) = 0$, demarcating the transition between negative and positive thermal expansions at a certain pressure, decreases as n increases (when materials of different layer numbers are compared at the same pressure). In each member of the homologous series, T_c increases with pressure. To understand the pressure effects and microscopic character of the phonon modes responsible for NTE in the homologous series, we next compute and show the Grüneisen-weighted phonon density of states in Fig. 7 according to

$$g_\gamma(\nu) = \frac{1}{N_q} \sum_{q,\sigma} \gamma_{q,\sigma} \delta(\nu - \nu_{q,\sigma}), \tag{5}$$

TABLE I. Critical pressures, temperatures, and phononic mechanism for NTE in the homologous series of calcium titanates. The critical temperatures listed are for the corresponding critical pressures of each material, but note that each pressure where NTE occurs will have its own critical temperature.

Material (n)	p_c (GPa)	T_c (K)	NTE mechanism
Ca_2TiO_4 (1)	5	146	Quasi-2D
$Ca_3Ti_2O_7$ (2)	10	49	Quasi-2D
$Ca_4Ti_3O_{10}$ (3)	13	19	Quasi-2D and quasi-RUM
$CaTiO_3$ (∞)	19.2	26	Quasi-RUM

at ambient (0 GPa) and high pressure (20 GPa). According to Eq. (4), we expect negative thermal expansion to occur when the number of occupied phonons with $\gamma < 0$ exceeds those exhibiting the usual positive behavior. At ambient pressure for each material, we find a net positive Grüneisen-weighted DOS, whereas at 20 GPa, it becomes negative for all materials. Thus, T_c increases with pressure because of the increased contribution of the negative Grüneisen DOS relative to the total as pressure increases (Fig. 7). This pressure dependence also manifests in the positive regions of $\alpha(T)$, which monotonically decrease as pressure increases. This reduction occurs due to bulk modulus stiffening (increasing) with pressure (Fig. 8), and the bulk modulus appears in the denominator of Eq. (4). Note that there is a slight negative value of the DOS for 0 GPa in Ca_2TiO_4 at low frequency, but that is due to the slightly negative frequencies appearing for the in-plane phonon dispersions (see Fig. S5 of the SI of Ref. [45]).

In all titanates, the positive Grüneisen modes blueshift to higher frequencies whereas negative Grüneisen modes redshift (Fig. S17 in the SI in Ref. [45], which plots the positive and negative contributions separately). In addition, the widths and magnitudes of the negative Grüneisen regions increase with pressure. This occurs in the Ruddlesden-Popper materials due to the membrane effect [25]. The shrinkage of the octahedral in-plane membrane area lowers the frequency of the quasi-2D mode and makes it more responsive to pressure (Fig. 9), resulting in a larger negative magnitude of the Grüneisen parameter. The pressure simultaneously shortens the interlayer spacing, evidenced by the compression of the average d spacing ($\bar{d}$, Fig. 9). This enhances the interlayer repulsion, hardening the ZA modes near the Γ point and reducing its anharmonicity.

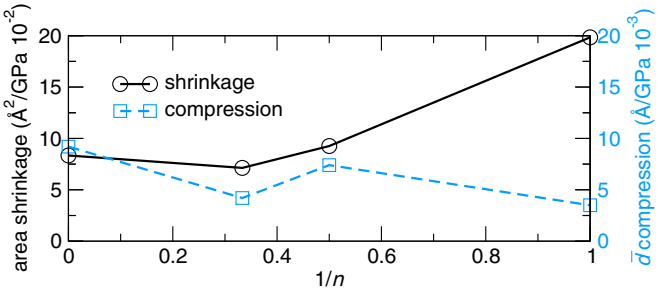

FIG. 9. (a) Octahedral in-plane membrane area shrinkage per applied pressure, and (b) the average d-spacing compression per applied pressure.

D. NTE capacity

To more clearly elucidate the effect of layer number n on the thermal expansion, we modify the recently defined metric called the NTE capacity [73]. Coates and Goodwin proposed the NTE capacity $\chi_v = -\alpha_v \Delta T$ as a feature to quantify and compare volumetric NTE across material families and mechanisms [73]. In this spirit, we introduced the integrated-NTE capacity as $\tilde{\chi}_v = -\int_{T_1}^{T_c} \alpha_v dT$ for noncubic materials where the temperature-dependent CTE is known. Note that in the definition of χ_v, a single CTE value is used to assess the complete temperature range (ΔT). As previously shown, the materials of the homologous calcium titanate series have different phononic mechanisms yielding NTE, making $\tilde{\chi}_v$ ideal for comparing NTE activity across the family as a function of layer number. With this feature, we find the integrated NTE capacity increases as layer number n decreases (Fig. 10). This can be understood in terms of the membrane effect wherein the thinner membrane (i.e., $n = 1$) is more responsive to external perturbations than a thicker membrane (i.e., $n = \infty$) and, thus, has larger NTE capacity. This result is consistent with our elasticity trends. The out-of-plane C_{33} and shearing C_{44} and C_{55} all increase as n increases. The elastically stiffer and thicker membrane limits the transverse vibration producing NTE via the tension mechanism. Here we note that whereas the Ca-Ti-O RP series exhibits pressure-induced NTE, the Sr-Ti-O series does not [23]. Electron-density profiles revealed that substitution of Ca by Sr stiffens the interfacial bonding (at the rocksalt motif), making the Sr-Ti-O series only have positive Grüneisen parameters and, thus, only positive thermal expansion (even under pressure).

E. Comparison of $P2_1/c$ and *Pbca* Ca_2TiO_4

We now examine the higher in energy but dynamically stable $n = 1$ $P2_1/c$ ambient pressure polymorph of Ca_2TiO_4 and compare it to the *Pbca* polymorph described previously. Crystallographic information for the monoclinic structure is available in the SI in Ref. [45]. Besides the monoclinic distortion along the stacking direction, the local connectivity of the two polymorphs are rather similar (Table II). They have almost the same average Ti-O bond length (including average axial and equatorial bond lengths), TiO octahedral volumes, and CaO polyhedral volumes. Additionally, the angles away from the [110] axis are also comparable. We also find that although $P2_1/c$ is less stiff than *Pbca* overall based on its bulk modulus value, there is no clear trend among the elastic constants (Table III).

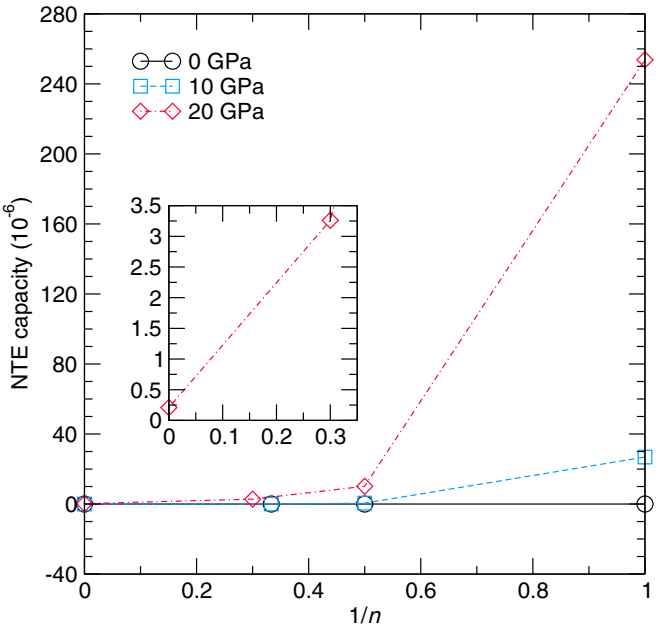

FIG. 10. Integrated NTE capacity for the CTO homologous series as a function of inverse layer number. As $1/n$ increases (i.e., n decreases) the integrated NTE capacity $\tilde{\chi}_v$ increases. The large value for the $n = 1$ *Pbca* phase is due to a dynamic instability of the phonons at 10 and 20 GPa; it is included here to reveal the NTE-capacity dependence with $1/n$.

In Fig. 11, we catalog lattice-dynamically derived properties of the $P2_1/c$ polymorph, including the (a) in-plane phonon spectra, (b) mode Grüneisen spectra, (c) comparison of the pressure-dependent cumulative sum of the Grüneisen-weighted phonon density of states (normalized per atom), and (d) pressure-dependent thermal expansion coefficient. Note that in this Brillouin zone, X corresponds to the reduced reciprocal point (0, 1/2, 0), A to (1/2, 1/2, 0), and Z to (1/2, 0, 0). These reciprocal space coordinates are on the plane defined by the perovskite TiO_6 layer. In contrast to *Pbca*, we do not find a nonlinear acoustic mode in the phonon spectra. Nonetheless, we do find a quasi-2D vibration leading to negative Grüneisen parameters as the ZA mode is negative at the Z point. It is hybridized with the LA mode, which has a positive-to-negative Grüneisen transition along Γ-Z due to the initial in-plane

TABLE II. Structural comparison of the $P2_1/c$ and *Pbca* Ca_2TiO_4 polymorphs using attributes defined in Fig. 2. The local connectivity in terms of bond lengths and polyhedral volumes and orientations are similar in both phases.

	$P2_1/c$	*Pbca*
$\bar{l}$ (Å)	1.95	1.95
$\bar{l}_{ax}$ (Å)	1.97	1.96
$\bar{l}_{eq}$ (Å)	1.94	1.95
Angle (°)	6.92	7.15
$\bar{V}_{TiO}$ (Å^3)	9.91	9.95
$\bar{V}_{CaO}$ (Å^3)	33.2	33.2

TABLE III. Elastic constant C_{ij} comparison of $n = 1$ Ca_2TiO_4 $P2_1c$ and *Pbca* polymorphs.

	Polymorph	
C_{ij} (GPa)	$P2_1/c$	*Pbca*
C_{11}	213.2	208.5
C_{22}	183.2	190.2
C_{33}	228.3	229.3
C_{44}	74.3	78.4
C_{55}	80.7	81.5
C_{66}	96.6	94.9
B	130.5	135.1

character followed by acquisition of the Z character along the path. This is similar to the Γ-X path of the *Pbca* structure where the quasi-2D modes with transverse eigenvectors led to negative Grüneisen parameters. Note that in both cases, the reciprocal path compared is $(0, 0, 0) \rightarrow (1/2, 0, 0)$.

The pressure-dependent positive and negative Grüneisen DOS yield different overall behaviors for the two polymorphs. Although the negative Grüneisen DOS increases for both polymorphs with pressure, the positive Grüneisen DOS shows opposite trends. The number of modes with $\gamma > 0$ in the $P2_1/c$ polymorph increases with pressure, whereas those in the *Pbca* decrease with pressure [Fig. 11(c)]. This can be rationalized with a representative example (whereas recognizing that the DOS depends on all modes) by considering a vibrational mode at $q = (1/2, 1/2, 0)$, i.e., the A point in $P2_1/c$. Here we find a mode with large positive character that is insensitive to pressure, whereas this feature and behavior is absent in *Pbca* at the corresponding (S) point [Fig. 6(a)].

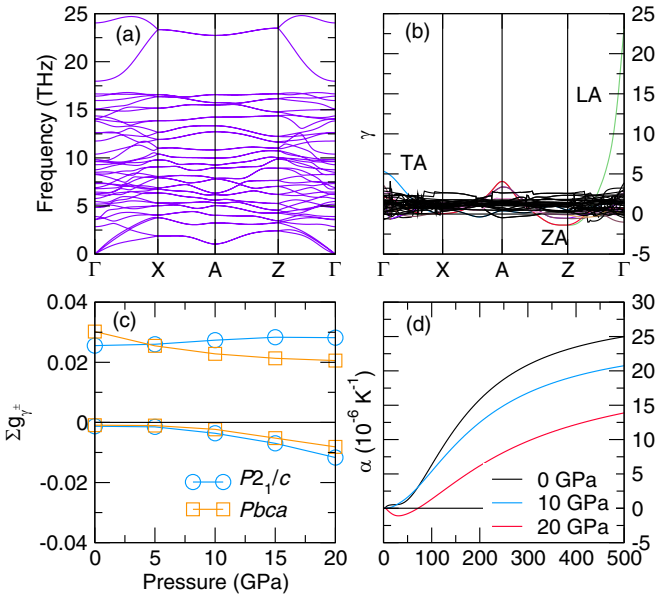

FIG. 11. Lattice dynamical properties for the $n = 1$ Ca_2TiO_4 $P2_1/c$ polymorph including the (a) in-plane phonon spectra, (b) mode Grüneisen spectra, with the ZA (red), TA (blue), and LA (green) modes labeled, (c) cumulative sum $P2_1/c$ and *Pbca* Grüneisen-weighted phonon density of states (normalized per atom) as a function of pressure, and (d) thermal expansion coefficient at various pressures.

Although NTE still appears in the $P2_1/c$ phase due to a quasi-2D mechanism, such as in the *Pbca* structure, it occurs at a critical pressure of 12 GPa (as opposed to $p_c = 5$ GPa in *Pbca*). This higher critical pressure occurs because of the persistent positive Grüneisen DOS in $P2_1/c$ that is absent in *Pbca* as noted earlier. This is additionally emphasized in Fig. S18 in the SI [45] where the Grüneisen DOS for $P2_1/c$ is shown in a decomposed and summed form. The summation is positive at pressures of 5 and 10 GPa but negative for 12 GPa (p_c) and 20 GPa. Importantly, the C_{33} for $P2_1/c$ is less than that of *Pbca*, suggesting that the elastic constants cannot be a universal descriptor for NTE behavior. In fact, the critical pressure of $n = 1$ $P2_1/c$ is greater than that of even the $n = 2$ $Ca_3Ti_2O_7$ (where $p_c = 10$ GPa).

The monoclinic angle seems to play a role in the different NTE behaviors. Specifically, the interlayer spacing of the Ca atoms in the rocksalt layers of $P2_1/c$ decreases faster with pressure than that in *Pbca* (4.7×10^{-3} Å/GPa vs 3.5×10^{-3} Å/GPa, respectively) thereby stiffening the ZA mode and contributing to the positive Grüneisen DOS population with pressure. Furthermore, although we find that the NTE mechanism of $P2_1/c$ is quasi-2D, a shearing-type mode which appears in the other orthorhombic RP members of the Ca-Ti-O series is not present in $P2_1/c$. The polymorph is already statically sheared in-plane along the long axis due to the monoclinic angle, and we find no vibrational mode with an eigenvector exhibiting a similar atomic displacement pattern. We know that NTE appears when there is more overall negative than positive Grüneisen DOS at certain frequencies. The shearing modes have large negative Grüneisen parameters in the orthorhombic RP systems, and, thus, the absence of it in the monoclinic structure in part justifies the higher NTE critical pressure in the $P2_1/c$ phase.

IV. CONCLUSIONS

We computed the temperature-dependent thermal expansion of the homologous series of Ruddlesden-Popper calcium titanate, $n = 1$–3, and ∞, using density functional theory methods. In the course of this paper, we predict dynamically stable Ca_2TiO_4 polymorphs thereby expanding the phase space of RP Ca-Ti-O materials. All structures exhibit positive thermal expansion at ambient conditions as well as pressure-induced negative thermal expansion, despite quadratic-dispersing phonons only appearing in the (orthorhombic) $n = 1$ and 2 phases. We found a quasi-2D NTE mechanism is active in the $n = 1$–3 phases, whereas the $n = \infty$ perovskite exhibits a quasi-RUM mechanism. Furthermore, we found trends with NTE and the layer number for the orthorhombic Ca-Ti-O RP series and introduced the integrated NTE capacity, which describes the volumetric contraction of a material over its NTE temperature range. The NTE trends are as follows: The NTE critical pressure increases as n increases, the NTE critical temperature decreases as n increases, and the NTE capacity decreases as n increases. This layer-dependent NTE behavior in the orthorhombic members is due to the increased lattice stiffness in the (out-of-plane) z direction as n increases as evidenced by changes in the elastic constants with layers n.

Our results suggest that less stiff (and thinner) RP and perovskite structures are more likely to have larger volumetric NTE capacity and, therefore, provide an important step forward in design of novel materials with tunable CTEs. Furthermore, our results suggest that for the same layer number n, stoichiometry, and chemical identity, a monoclinic angle will reduce NTE behavior. Fully anisotropic volume expansion, which may yield axis-specific trends for this series, could be pursued in future work.

ACKNOWLEDGMENTS

N.Z.K. and J.M.R. acknowledge support from the U.S. Department of Energy (DOE) under Grant No. DE-SC0012375. This work used the Quest cluster at Northwestern University, the DOD HPCMP, and the National Energy Research Scientific Computing Center, a DOE Office of Science User Facility supported by the Office of Science of the U.S. Department of Energy under Contract No. DE-AC02-05CH11231.

[1] Y. Liu, N. O. Weiss, X. Duan, H.-C. Cheng, Y. Huang, and X. Duan, Van der waals heterostructures and devices, Nat. Rev. Mater. **1**, 16042 (2016).

[2] D. I. Khomskii and T. Mizokawa, Orbitally Induced Peierls State in Spinels, Phys. Rev. Lett. **94**, 156402 (2005).

[3] I. I. Mazin, H. O. Jeschke, K. Foyevtsova, R. Valentí, and D. I. Khomskii, Na_2IrO_3 as a Molecular Orbital Crystal, Phys. Rev. Lett. **109**, 197201 (2012).

[4] G. Plechinger, F.-X. Schrettenbrunner, J. Eroms, D. Weiss, C. Schüller, and T. Korn, Low-temperature photoluminescence of oxide-covered single-layer MoS_2, Phys. Status Solidi RRL **6**, 126 (2012).

[5] K. Sano, T. Takahashi, and K. Uchida, Large variability of contact resistance in Au/Cr/MoS_2 system and its suppression by Cr thinning, Jpn. J. Appl. Phys. **55**, 036501 (2016).

[6] D. Yoon, Y. W. Son, and H. Cheong, Negative thermal expansion coefficient of graphene measured by raman spectroscopy, Nano Lett. **11**, 3227 (2011).

[7] T. Yokoyama and K. Eguchi, Anisotropic Thermal Expansion and Cooperative Invar and Anti-Invar Effects in Mn Alloys, Phys. Rev. Lett. **110**, 075901 (2013).

[8] X.-J. Ge, K.-L. Yao, and J.-T. Lü, Comparative study of phonon spectrum and thermal expansion of graphene, silicene, germanene, and blue phosphorene, Phys. Rev. B **94**, 165433 (2016).

[9] Z.-Y. Wang, Y.-L. Zhou, X.-Q. Wang, F. Wang, Q. Sun, Z.-X. Guo, and Y. Jia, Effects of in-plane stiffness and charge transfer on thermal expansion of monolayer transition metal dichalcogenide, Chin. Phys. B **24**, 026501 (2015).

[10] N. Mounet and N. Marzari, First-principles determination of the structural, vibrational and thermodynamic properties of diamond, graphite, and derivatives, Phys. Rev. B **71**, 205214 (2005).

[11] C. A. Occhialini, G. G. Guzmn-Verri, S. U. Handunkanda, and J. N. Hancock, Negative thermal expansion near the precipice of structural stability in open perovskites, Front. Chem. **6**, 545 (2018).

[12] K. Takenaka, Progress of research in negative thermal expansion materials: Paradigm shift in the control of thermal expansion, Front. Chem. **6**, 267 (2018).

[13] Y. Oba, T. Tadano, R. Akashi, and S. Tsuneyuki, First-principles study of phonon anharmonicity and negative thermal expansion in ScF_3, Phys. Rev. Materials **3**, 033601 (2019).

[14] C. Ablitt, S. Craddock, M. S. Senn, A. A. Mostofi, and N. C. Bristowe, The origin of uniaxial negative thermal expansion in layered perovskites, npj Comput. Mater. **3**, 44 (2017).

[15] E. T. Ritz and N. A. Benedek, Interplay Between Phonons and Anisotropic Elasticity Drives Negative Thermal Expansion in $PbTiO_3$, Phys. Rev. Lett. **121**, 255901 (2018).

[16] M. T. Dove and H. Fang, Negative thermal expansion and associated anomalous physical properties: review of the lattice dynamics theoretical foundation, Rep. Prog. Phys. **79**, 066503 (2016).

[17] J. S. O. Evans, Negative thermal expansion materials, J. Chem. Soc. Dalton Trans., 3317 (1999).

[18] G. D. Barrera, J. A. O. Bruno, T. H. K. Barron, and N. L. Allan, Negative thermal expansion, J. Phys.: Condens. Matter **17**, R217 (2005).

[19] S. d'Ambrumenil, M. Zbiri, A. M. Chippindale, S. J. Hibble, E. Marelli, and A. C. Hannon, Lattice dynamics and negative thermal expansion in the framework compound $ZnNi(CN)_4$ with two-dimensional and three-dimensional local environments, Phys. Rev. B **99**, 024309 (2019).

[20] C.-H. Lee, N. J. Podraza, Y. Zhu, R. F. Berger, S. Shen, M. Sestak, R. W. Collins, L. F. Kourkoutis, J. A. Mundy, H. Wang, Q. Mao, X. Xi, L. J. Brillson, J. B. Neaton, D. A. Muller, and D. G. Schlom, Effect of reduced dimensionality on the optical band gap of $SrTiO_3$, Appl. Phys. Lett. **102**, 122901 (2013).

[21] S. E. Reyes-Lillo, T. Rangel, F. Bruneval, and J. B. Neaton, Effects of quantum confinement on excited state properties of $SrTiO_3$ from ab initio many-body perturbation theory, Phys. Rev. B **94**, 041107(R) (2016).

[22] T. Birol, N. A. Benedek, and C. J. Fennie, Interface Control of Emergent Ferroic Order in Ruddlesden-Popper $Sr_{n+1}Ti_nO_{3n+1}$, Phys. Rev. Lett. **107**, 257602 (2011).

[23] L.-F. Huang, N. Z. Koocher, M. Gu, and J. M. Rondinelli, Structure dependent phase stability and thermal expansion of ruddlesdenpopper strontium titanates, Chem. Mater. **30**, 7100 (2018).

[24] J. G. Cherian, T. Birol, N. C. Harms, B. Gao, S.-W. Cheong, D. Vanderbilt, and J. L. Musfeldt, Optical spectroscopy and band gap analysis of hybrid improper ferroelectric $Ca_3Ti_2O_7$, Appl. Phys. Lett. **108**, 262901 (2016).

[25] L.-F. Huang, X.-Z. Lu, and J. M. Rondinelli, Tunable Negative Thermal Expansion in Layered Perovskites from Quasi-Two-Dimensional Vibrations, Phys. Rev. Lett. **117**, 115901 (2016).

[26] D. Bansal, J. L. Niedziela, X. He, T. Lanigan-Atkins, A. Said, A. Alatas, D. L. Abernathy, Y. Ren, B. Gao, S.-W. Cheong, and O. Delaire, Lattice dynamics of the hybrid improper ferroelectrics $(Ca, Sr)_3ti_2o_7$, Phys. Rev. B **100**, 214304 (2019).

[27] M. S. Senn, A. Bombardi, C. A. Murray, C. Vecchini, A. Scherillo, X. Luo, and S. W. Cheong, Negative Thermal Expansion in Hybrid Improper Ferroelectric Ruddlesden-Popper

Perovskites by Symmetry Trapping, Phys. Rev. Lett. **114**, 035701 (2015).

[28] M. S. Senn, C. A. Murray, X. Luo, L. Wang, F. T. Huang, S. W. Cheong, A. Bombardi, C. Ablitt, A. A. Mostofi, and N. C. Bristowe, Symmetry switching of negative thermal expansion by chemical control, J. Am. Chem. Soc. **138**, 5479 (2016).

[29] C. Ablitt, A. A. Mostofi, N. C. Bristowe, and M. S. Senn, Control of uniaxial negative thermal expansion in layered perovskites by tuning layer thickness, Front. Chem. **6**, 455 (2018).

[30] C. Ablitt, H. McCay, S. Craddock, L. Cooper, E. Reynolds, A. A. Mostofi, N. C. Bristowe, C. A. Murray, and M. S. Senn, Tolerance factor control of uniaxial negative thermal expansion in a layered perovskite, Chemistry of Materials, Chem. Mater. **32**, 605 (2020).

[31] N. A. Benedek, J. M. Rondinelli, H. Djani, P. Ghosez, and P. Lightfoot, Understanding ferroelectricity in layered perovskites: New ideas and insights from theory and experiments, Dalton Trans. **44**, 10543 (2015).

[32] A. M. Glazer, The classification of tilted octahedra in perovskites, Acta Crystallogr., Sect. B: Struct. Crystallogr. Cryst. Chem. **28**, 3384 (1972).

[33] R. Ali and M. Yashima, Space group and crystal structure of the perovskite $CaTiO_3$ from 296 to 1720 K, J. Solid State Chem. **178**, 2867 (2005).

[34] M. Yashima and R. Ali, Structural phase transition and octahedral tilting in the calcium titanate perovskite $CaTiO_3$, Solid State Ionics **180**, 120 (2009).

[35] M. Guennou, P. Bouvier, B. Krikler, J. Kreisel, R. Haumont, and G. Garbarino, High-pressure investigation of $CaTiO_3$ up to 60 GPa using x-ray diffraction and Raman spectroscopy, Phys. Rev. B **82**, 134101 (2010).

[36] A. M. Teweldeberhan, J. L. Dubois, and S. A. Bonev, Stability of the high-pressure phases of $CaTiO_3$ perovskite at finite temperatures, Phys. Rev. B **86**, 064104 (2012).

[37] M. M. Elcombe, E. H. Kisi, K. D. Hawkins, T. J. White, P. Goodman, and S. Matheson, Structure determinations for $Ca_3Ti_2O_7$, $Ca_4Ti_3O_{10}$, $Ca_{3.6}Sr_{0.4}Ti_3O_{10}$ and a refinement of $Sr_3Ti_2O_7$, Acta Crystallographica Section B **47**, 305 (1991).

[38] N. A. Benedek and C. J. Fennie, Hybrid Improper Ferroelectricity: A Mechanism for Controllable Polarization-Magnetization Coupling, Phys. Rev. Lett. **106**, 107204 (2011).

[39] A. H. Ramadan, L. Hesselmann, and R. A. De Souza, The phase stability of Ca_2TiO_4 and related Ruddlesden-Popper phases, J. Phys. Chem. Solids **86**, 90 (2015).

[40] K. T. Jacob and S. Gupta, Phase diagram of the system Ca-Ti-O at 1200 K, Bull. Mater. Sci. **32**, 611 (2009).

[41] J. E. Saal, S. Kirklin, M. Aykol, B. Meredig, and C. Wolverton, Materials design and discovery with high-throughput density functional theory: The open quantum materials database (OQMD), JOM **65**, 1501 (2013).

[42] S. Kirklin, J. E. Saal, B. Meredig, A. Thompson, J. W. Doak, M. Aykol, S. Rühl, and C. Wolverton, The Open Quantum Materials Database (OQMD): Assessing the accuracy of DFT formation energies, npj Comput. Mater. **1**, 15010 (2015).

[43] W. Gong, L. Wu, and A. Navrotsky, Combined experimental and computational investigation of thermodynamics and phase equilibria in the caotio2 system, J. Am. Ceram. Soc. **101**, 1361 (2018).

[44] P. V. Balachandran, D. Puggioni, and J. M. Rondinelli, Crystal-chemistry guidelines for noncentrosymmetric a_2bo_4 ruddlesden-popper oxides, Inorg. Chem. **53**, 336 (2014).

[45] See Supplemental Material at http://link.aps.org/supplemental/10.1103/PhysRevMaterials.5.053601 for computational details. It includes a comparison of experimental and DFT-relaxed structures, phonons and an energy ranking of possible $n = 1$ Ca_2TiO_4 polymorphs, Birch-Murnaghan equation of states, and $E(V)$ curves, lattice constants of the $n = 1$ *Pbca* phase under pressure, lattice dynamics of $n = 1$ *Pbca* obtained with different calculation parameters, $n = 1$ *Cmca* phonons, $n = 3$ phonons as a function of pressure, a comparison of material volumes as calculated by DFT and the SC-QHA method, details of the SC-QHA method applied to the $n = 3$ compound, atomic displacement images for phonon modes which have large Grüneisen parameters for each material, decomposed Grüneisen-weighted phonon DOS into positive and negative components, and a comparison of our calculated thermal expansion coefficient with experimental values from the literature. It includes Refs. [63–67] not cited in the main text. There is also a Supplemental animation online of the quasi-RUM occurring in the $n = 3$ structure.

[46] J. P. S. Walsh, S. M. Clarke, Y. Meng, S. D. Jacobsen, and D. E. Freedman, Discovery of $FeBi_2$, ACS Central Sci. **2**, 867 (2016).

[47] K. M. Powderly, S. M. Clarke, M. Amsler, C. Wolverton, C. D. Malliakas, Y. Meng, S. D. Jacobsen, and D. E. Freedman, High-pressure discovery of β-nibi, Chem. Commun. **53**, 11241 (2017).

[48] A. D. Tamerius, S. M. Clarke, M. Gu, J. P. S. Walsh, M. Esters, Y. Meng, C. H. Hendon, J. M. Rondinelli, S. D. Jacobsen, and D. E. Freedman, Discovery of Cu_3Pb, Ange. Chem., Int. Ed. **57**, 12809 (2018).

[49] A. B. Altman, A. D. Tamerius, N. Z. Koocher, Y. Meng, C. J. Pickard, J. P. S. Walsh, J. M. Rondinelli, S. D. Jacobsen, and D. E. Freedman, Computationally directed discovery of $MoBi_2$, J. Am. Chem. Soc. **143**, 214 (2021).

[50] C. L. Tracy, S. Park, D. R. Rittman, S. J. Zinkle, H. Bei, M. Lang, R. C. Ewing, and W. L. Mao, High pressure synthesis of a hexagonal close-packed phase of the high-entropy alloy CrMnFeCoNi, Nat. Commun. **8**, 15634 (2017).

[51] G. Kresse and J. Furthmüller, Efficiency of ab-initio total energy calculations for metals and semiconductors using a plane-wave basis set, Comput. Mater. Sci. **6**, 15 (1996).

[52] G. Kresse and J. Furthmüller, Efficient iterative schemes for ab initio total-energy calculations using a plane-wave basis set, Phys. Rev. B **54**, 11169 (1996).

[53] P. E. Blöchl, Projector augmented-wave method, Phys. Rev. B **50**, 17953 (1994).

[54] G. Kresse and D. Joubert, From ultrasoft pseudopotentials to the projector augmented - wave method, Phys. Rev. B **59**, 1758 (1999).

[55] J. P. Perdew, K. Burke, and M. Ernzerhof, Generalized Gradient Approximation Made Simple, Phys. Rev. Lett. **77**, 3865 (1996).

[56] J. P. Perdew, K. Burke, and M. Ernzerhof, Generalized Gradient Approximation Made Simple [Phys. Rev. Lett. 77, 3865 (1996)], Phys. Rev. Lett. **78**, 1396 (1997).

[57] A. Togo and I. Tanaka, First principles phonon calculations in materials science, Scr. Mater. **108**, 1 (2015).

[58] W. Setyawan and S. Curtarolo, High-throughput electronic band structure calculations: Challenges and tools, Comput. Mater. Sci. **49**, 299 (2010).

[59] L.-F. Huang, X.-Z. Lu, E. Tennessen, and J. M. Rondinelli, An efficient ab-initio quasiharmonic approach for the thermodynamics of solids, Comput. Mater. Sci. **120**, 84 (2016).

[60] S. Baroni, P. Giannozzi, and E. Isaev, Density-functional perturbation theory for quasi-harmonic calculations, Rev. Mineral. Geochem. **71**, 39 (2010).

[61] A. Togo, L. Chaput, I. Tanaka, and G. Hug, First-principles phonon calculations of thermal expansion in ti_3sic_2, ti_3alc_2, and ti_3gec_2, Phys. Rev. B **81**, 174301 (2010).

[62] The SC-QHA code is available at the GitHub Page: https://github.com/MTD-group/Self-Consistent-Quasiharmonic-Approximation-Method.

[63] P. Nath, D. Usanmaz, D. Hicks, C. Oses, M. Fornari, M. Buongiorno Nardelli, C. Toher, and S. Curtarolo, Aflow-qha3p: Robust and automated method to compute thermodynamic properties of solids, Phys. Rev. Materials **3**, 073801 (2019).

[64] S. L. Shang, Y. Wang, D. E. Kim, and Z. K. Liu, First-principles thermodynamics from phonon and Debye model: Application to Ni and Ni_3Al, Comput. Mater. Sci. **47**, 1040 (2010).

[65] L. F. Huang, P. L. Gong, and Z. Zeng, Correlation between structure, phonon spectra, thermal expansion, and thermomechanics of single-layer mos_2, Phys. Rev. B **90**, 045409 (2014).

[66] W. Utsumi, N. Funamori, T. Yagi, E. Ito, T. Kikegawa, and O. Shimomura, Thermal expansivity of $MgSiO_3$ perovskite under high pressures up to 20 GPa, Geophys. Res. Lett. **22**, 1005 (1995).

[67] N. Funamori and T. Yagi, High pressure and high temperature in situ X-ray observation of $MgSiO_3$ Perovskite under lower mantle conditions, Geophys. Res. Lett. **20**, 387 (1993).

[68] Y. Takubo, H. Terasaki, T. Kondo, S. Mitai, S. Kamada, T. Kikegawa, and A. Machida, Variations of lattice constants and thermal expansion coefficients of indium at high pressure and high temperature, High Press. Res. **38**, 406 (2018).

[69] N. Funamori, T. Yagi, and T. Uchida, High-pressure and high-temperature in situ x-ray Diffraction study of iron to above 30 Gpa using MA8-type apparatus, Geophys. Res. Lett. **23**, 953 (1996).

[70] K. M. Hope, G. K. Samudrala, and Y. K. Vohra, Near-zero thermal expansion in magnetically ordered state in dysprosium at high pressures and low temperatures, Cogent Physics **4**, 1412107 (2017).

[71] A. Dewaele and G. Garbarino, Low temperature equation of state of iron, Appl. Phys. Lett. **111**, 021903 (2017).

[72] L. Hu, F. Qin, A. Sanson, L.-F. Huang, Z. Pan, Q. Li, Q. Sun, L. Wang, F. Guo, U. Aydemir, Y. Ren, C. Sun, J. Deng, G. Aquilanti, J. M. Rondinelli, J. Chen, and X. Xing, Localized symmetry breaking for tuning thermal expansion in ScF_3 nanoscale frameworks, J. Am. Chem. Soc. **140**, 4477 (2018).

[73] C. S. Coates and A. L. Goodwin, How to quantify isotropic negative thermal expansion: Magnitude, range, or both?, Mater. Horiz. **6**, 211 (2019).